algorithms

MDPI

Article

Remote Sensing of Snow Parameters: A Sensitivity Study of Retrieval Performance Based on Hyperspectral versus Multispectral Data

Elliot Pachniak [1,*], Wei Li [1], Tomonori Tanikawa [2], Charles Gatebe [3] and Knut Stamnes [1]

[1] Light and Life Laboratory, Physics Department, Stevens Institute of Technology, Hoboken, NJ 07030, USA; wli4@stevens.edu (W.L.); kstamnes@stevens.edu (K.S.)
[2] Meteorological Research Institute, Japan Meteorological Agency, Tsukuba 3050052, Ibaraki, Japan; tanikawa@mri-jma.go.jp
[3] NASA Ames Research Center, Moffett Field, CA 94035, USA; charles.k.gatebe@nasa.gov
* Correspondence: epachnia@stevens.edu

Abstract: Snow parameters have traditionally been retrieved using discontinuous, multi-band sensors; however, continuous hyperspectral sensors are now being developed as an alternative. In this paper, we investigate the performance of various sensor configurations using machine learning neural networks trained on a simulated dataset. Our results show improvements in the accuracy of retrievals of snow grain size and impurity concentration for continuous hyperspectral channel configurations. Retrieval accuracy of snow albedo was found to be similar for all channel configurations.

Keywords: snow; neural networks; remote sensing; hyperspectral; machine learning; MODIS; SGLI; SBG DO

Citation: Pachniak, E.; Li, W.; Tanikawa, T.; Gatebe, C.; Stamnes, K. Remote Sensing of Snow Parameters: A Sensitivity Study of Retrieval Performance Based on Hyperspectral versus Multispectral Data. *Algorithms* **2023**, *16*, 493. https://doi.org/10.3390/a16100493

Academic Editor: Matteo Diez

Received: 15 September 2023
Revised: 19 October 2023
Accepted: 20 October 2023
Published: 23 October 2023

1. Introduction

Long-term global mapping of snow albedo and snow property parameters plays an important role in monitoring of the Earth climate system. Satellite remote sensing has offered a very valuable and powerful way to record the extent of the evolution of global snow and properties with high temporal and spatial resolution [1–3]. The visible and near-infrared bands can be used to obtain snow coverage, broadband albedo, and snow physical parameters [4–7].

The Surface Biology and Geology (SBG) Designated Targeted Observable (DO) [8] is a proposed sensor based on the need for capabilities to acquire global, high spatial resolution, visible to shortwave infrared (VSWIR; 380–2500 nm; 30 m pixel resolution, 10 nm spectral resolution) hyperspectral (imaging spectroscopy) and multispectral midwave and thermal infrared (MWIR: 3–5 µm; TIR: 8–12 µm; ∼60 m pixel resolution) measurements with sub-monthly temporal revisits. These specifications were proposed to meet the goals laid out by the 2017–2027 Decadal Survey, *Thriving on our Changing Planet* [9], which places a high-priority emphasis on global-scale inquiries into hydrology, ecosystems, weather, climate, and solid earth. An SBG Algorithms Working Group of multidisciplinary researchers was formed to review and evaluate the algorithms applicable to the SBG DO across a wide range of Earth science disciplines, including terrestrial and aquatic ecology, atmospheric science, geology, and hydrology.

Traditionally, data from the MODIS and SGLI sensors have been used to provide global maps of snow cover [10–12]. However, both MODIS and SGLI are discontinuous multi-band radiometers with isolated 50–100 nm-wide spectral bands, whereas the SBG VSWIR instrument is envisioned to provide continuous spectral coverage from 380 to 2500 nm with 10 nm spectral resolution. The combination of improved spectral resolution and continuous spectral coverage has been shown to increase information content and spectral dimensionality leading to improvements in atmospheric correction when compared to

multi-band approaches [13]. It has been proposed that hyperspectral data can leverage the entire spectrum to more accurately determine snow albedo, grain size, cloud cover over snow, and unmixed pixels containing both vegetation and snow [14].

Key features of our methodology for snow parameter retrieval (SPR) include (i) use of a coupled atmosphere–surface radiative transfer (RT) model to create a large simulated dataset of top of the atmosphere (TOA) reflectances as a function of snow and aerosol physical parameters; (ii) use of this simulated dataset to train a multi layer neural network (MLNN) for the retrieval, which has led to significant improvements in both retrieval accuracy and speed; and (iii) use of an aaNN filtered (instead of a random) distribution of snow and aerosol parameters to generate the synthetic dataset used for MLNN training, which mimics a more realistic snow situation, and leads to significantly improved retrievals.

Our goal is to explore the possible improvements to our SPR algorithms from leveraging continuous spectral coverage from 380 to 2500 nm. Section 2 describes the motivation and formation of our snow dataset. Section 3 details our scientific machine learning (SciML) neural network algorithm methodology and training. Section 4 presents our sensitivity study findings and a discussion of results. Concluding remarks are provided in Section 5.

2. Models and Data

2.1. Motivation

Snow interacts strongly with the global climate system, serving as an energy bank [15,16], radiation shield [17], insulator [18], reservoir [19], and transport medium [20–22]. For these reasons, it is vitally important to understand and accurately measure the physical properties of snow.

An important parameter in climate research is the ratio of reflected light to the incoming global shortwave radiation, also know as the albedo [23]. For a given spectral distribution of the incoming solar radiation, the albedo of a homogeneous sufficiently thick snow layer depends mainly on snow quality, which can be described by the type of snow (snow density and grain size) [24] and its impurity concentration (concentration of light absorbing particles in the snow, such as black carbon or dust) [25]. Since snow grain size and impurity content change over time, the albedo of a snow-packed region often decreases with time until it is refreshed by new snowfall [26]. This cycle can be used to determine the melting processes of a snow-packed region as well as the monitoring of snow accumulation from remote sensing data collected by sensors deployed on satellites.

Light from the sun will be absorbed and scattered in predictable ways depending on the snow's physical and optical properties. Remote sensing instruments deployed on satellites can collect reflected radiances at the top of the atmosphere. These TOA radiances depend on snow properties as well as the sun-satellite geometry, i.e., the solar zenith angle, the sensor polar viewing angle, and the relative azimuth angle. A radiative transfer tool can be used to model these TOA radiances as a function of wavelength. A flowchart summarizing the methods used in data formation, modeling, and algorithm formation is shown in Figure 1.

2.2. Radiative Transfer Model: AccuRT

AccuRT is an accurate, efficient, and easy-to-use radiative transfer simulation tool that can be used to generate radiance and irradiance data at user-defined vertical locations in a coupled atmosphere–water system [27]. Note here that "water" refers to both the liquid and solid phase (snow and ice). The physical properties of each of the two slabs that constitute the coupled system, the radiative energy input at the top of the upper slab (TOA), and the boundary conditions at the bottom of the lower slab (water bottom) must be specified. To facilitate these specifications, AccuRT uses a set of radiatively significant constituents called "materials" that account for the wavelength dependence of inherent optical properties (IOPs). For our simulated dataset, we include the *earth_atmospheric_gases*, *aerosols*, and *snow* materials in our main configuration file. The wavelength range was specified to be 380–2500 nm with 10 nm spacing to meet the needs of NASA's Ames Global

Hyperspectral Synthetic Data [28]. Once the input parameters have been specified, the AccuRT code will solve the radiative transfer equation and provide irradiances at desired vertical locations as well as radiances at desired vertical locations and in desired directions in the coupled atmosphere–snow system. In our case, the desired location for irradiances is the top of the snow layer, where the ratio of the upward and downward spectral irradiance is used to compute the spectral snow albedo. The input solar spectrum at the top-of-the-atmosphere (TOA) is ATLAS-3 (shifted to air wavelengths) for 200 nm to 407 nm, ATLAS-2 for 407.8 nm to 419.9 nm, and MODTRAN (v3.5) for 419.9 nm to 800 nm [29,30]. Between 200 and 800 nm, the solar irradiance has a spectral resolution of 0.05 nm. For wavelengths of 800 nm, the ASTM G173-03 [31] spectrum is adopted with a spectral resolution of 1 nm between 800 nm and 1700 nm and 5 nm between 1700 nm and 4000 nm. For radiances, we want the upward radiance at the TOA in specified directions that would correspond to a desired sun-satellite geometry (solar zenith angle, observation polar angle, and relative azimuth angle) and snow grain size and impurity concentration. A pixel in a satellite image obtained over a snow surface is defined by these five parameters.

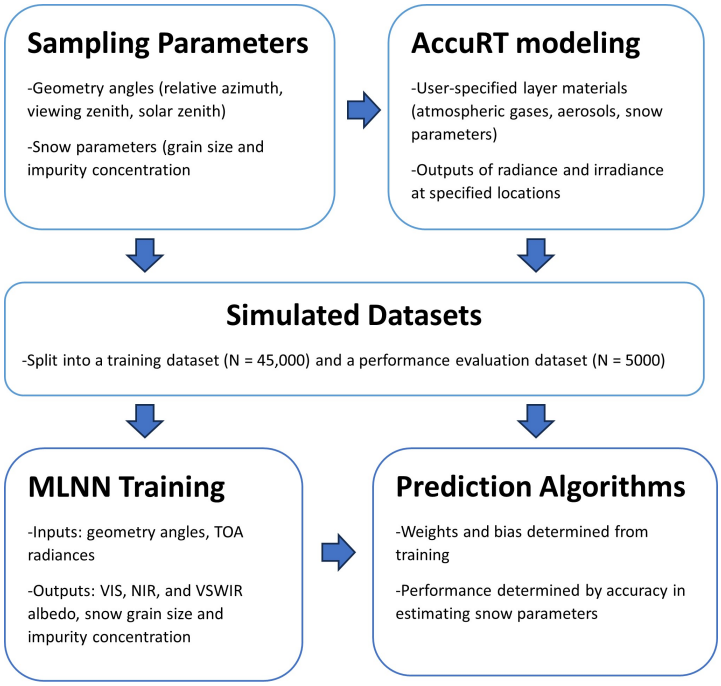

Figure 1. Framework used in data formation, modeling, and algorithm formation. Descriptions of each step are provided in the following sections.

2.2.1. Atmospheric Gases

The *earth_atmospheric_gases* material allows the user to choose from six model atmospheres. For our purposes, we have chosen the US 1976 standard [32] model. All of the models are based on the best information available when they were published and contain altitude profiles of temperature, pressure, and concentrations of the bulk atmospheric molecules (N_2 and O_2), as well as many radiatively significant trace gases including H_2O, CO_2, O_3, CH_4, and NO_2. From this material, we obtain the specifications of absorption coefficients for the radiatively significant atmospheric gases based on the LowTran/ModTran band model. Molecular (Rayleigh) scattering coefficients are also provided by the *earth_atmospheric_gases* material.

2.2.2. Atmospheric Aerosols

The *aerosols* material provides a convenient way to specify the aerosol properties as a function of wavelength based on a bi-modal particle size distribution including a fine and a coarse mode. The user specifies the vertical profile of the aerosols in the atmosphere,

as well as the refractive index (real and imaginary parts), the effective radii, and the variances of the two modes. Then, a Mie scattering code is used to compute the IOPs of aerosol particles and a numerical integration is employed to integrate over the log-normal size distributions to obtain the absorption and scattering coefficients and the scattering phase function. For our configuration, fine mode aerosols have an optical depth of 0.212 and a single-scattering albedo of 0.948, while coarse mode aerosols have an optical depth of 0.026 and a single-scattering albedo of 1 at a reference wavelength λ = 500 nm. These values are consistent with values typically measured in the atmosphere [33].

2.2.3. Snow Properties

We assume a spherical particle shape for snow grains, which allows us to obtain their IOPs from a parameterized Mie scattering model. We use the ISIOP tool [34] to generate ice/snow IOPs for any desired wavelength from ice/snow physical parameters: real and imaginary parts of the ice/snow refractive index, asymmetry factors for scattering by snow grains, and the snow layer thickness. The parameterized Mie scattering model relies on the assumptions that the snow particles (i) can be characterized by an effective radius, (ii) are weakly absorbing, and (iii) are large compared to the wavelength of light. These assumptions imply that the calculations of the absorption and scattering coefficients and the scattering asymmetry factor can be greatly simplified. Also, the scattering phase function is approximated by the Henyey–Greenstein function, which depends only on the scattering asymmetry factor, and snow impurities are included to account for absorbing material deposited in the snowpack. This approach leads to the computed snow albedo values in agreement with available observations [35].

2.3. Synthetic Snow Dataset

2.3.1. Random Data

Fifty-thousand values for the relative azimuth angle, viewing zenith angle, solar zenith angle, snow grain size, and impurity concentration were used to generate a synthetic training dataset. The angular data were formed with a uniform random distribution in the solar zenith angle, viewing polar angle, and relative azimuth angle, while the grain size and the impurity concentration were formed with a log-normal random distribution. The log-normal distributions were chosen to cluster random data around values that are more likely to be found in nature. A summary of the dataset is shown in Table 1. This dataset was used to simulate radiances and irradiances, employing the AccuRT computational tool.

Table 1. Summary of parameters used to generate the synthetic training dataset.

Parameter	Data Range	Distribution	Mean
Relative azimuth angle	0 to 180 (degrees)	Uniform	89.87°
Viewing zenith angle	0 to 45 (degrees)	Uniform	22.55°
Solar zenith angle	20 to 75 (degrees)	Uniform	47.62°
Snow grain size	50 to 2500 (µm)	Log-normal	835 µm
Snow impurity concentration	10^{-9} to 10^{-5} (ratio)	Log-normal	9.27×10^{-8}

2.3.2. Illustrative Examples

To gain a sense of how the various parameters affect radiances and the albedo, several computations were carried out at designated 10 nm increments of the parameter values. To this end, radiance versus wavelength plots for upward radiances at the TOA are provided in Figure 2. Also, albedo versus wavelength plots for varying solar zenith angle, snow grain size, and impurity concentration are provided in Figure 3. Figure 2 shows that variability in radiance is largely affected by the solar zenith angle and snow grain size, with the impurity concentration also having a significant impact in the visible part of the spectrum. Changes to the relative azimuth and viewing zenith angle have a relatively minimal observable effect on the TOA radiance; however, the forward reflection (BRDF)

is generally stronger, especially along the principal in NIR, which can lead to significant differences depending on the viewing/azimuth angles. Figure 3 shows that these findings are also true for the snow surface albedo. It is worth noting that only snow grain size seems to have a significant impact on radiance past 1500 nm, and only when the grain size is quite small, in the 50–300 µm range. Impurity concentration has the biggest impact on the albedo for wavelengths in the visible part of the spectrum, while a decrease in snow grain size caused the albedo to increase. This albedo enhancement is most dramatic in the near-infrared nm range. Changes in the solar zenith angle cause noticeable changes in the albedo across all wavelengths.

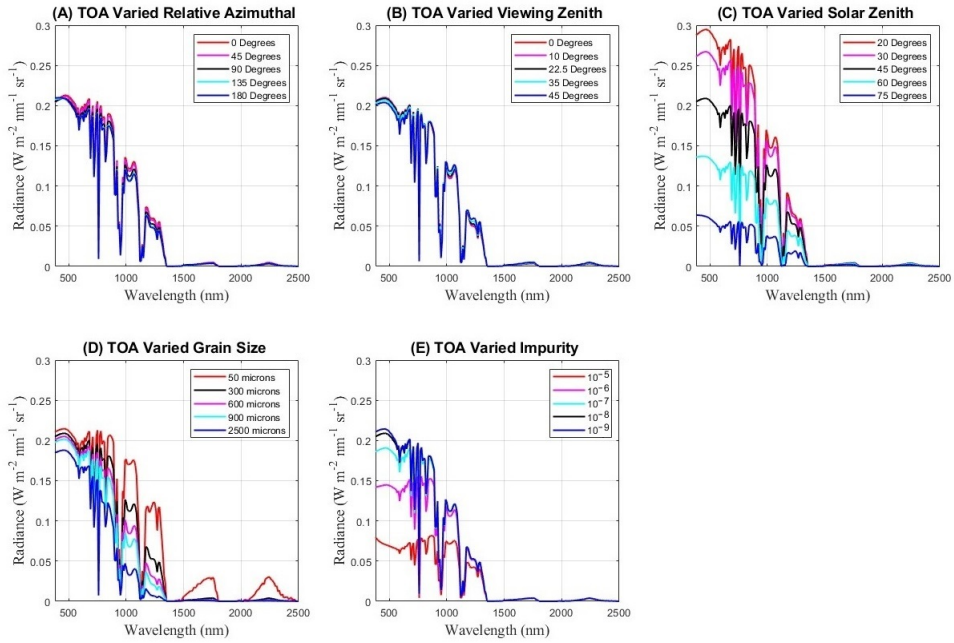

Figure 2. Radiance vs. wavelength plots at TOA, the black lines in all plots have constant relative azimuthal angle of 90°, viewing zenith angle of 22.5°, solar zenith angle of 45°, grain size of 300 µm, and impurity concentration of 10^{-8}. In all plots, four of the parameters are held to the constant values listed above, while the fifth is varied. (**A**) Varied relative azimuthal angles from 0 to 180°. (**B**) Varied viewing zenith angles from 0° to 45°. (**C**) Varied solar zenith angles from 20° to 75°. (**D**) Varied snow grain size from 50 to 2500 µm. (**E**) Varied impurity concentration from 10^{-9} to 10^{-5}.

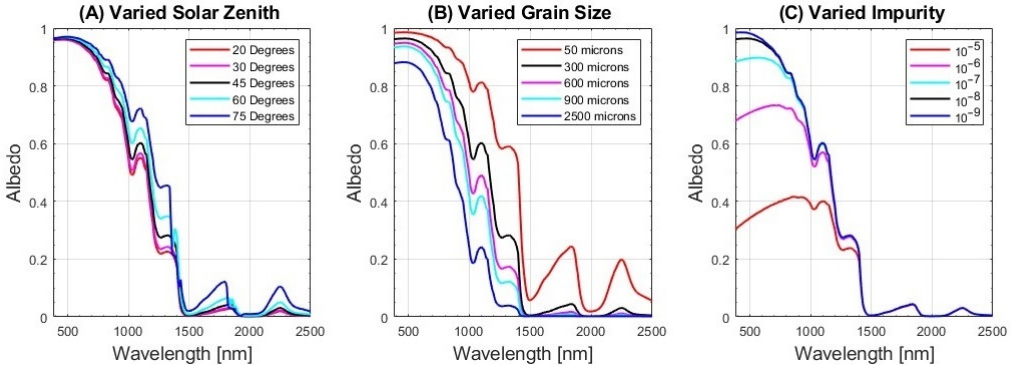

Figure 3. Albedo vs. wavelength plots for a variety of conditions. The black lines in all plots have constant relative azimuthal angle of 90°, viewing zenith angle of 22.5°, solar zenith angle of 45°, grain size of 300 µm, and impurity concentration of 10^{-8}. In all plots, four of the parameters are held to the constant values listed above, while the fifth is varied. (**A**) Varied solar zenith angles from 20 to 75°. (**B**) Varied snow grain size from 50 to 2500 µm. (**C**) Varied impurity concentration from 10^{-9} to 10^{-5}.

3. Methods

3.1. Multi-Layer Neural Networks

We want to use the synthetic dataset to retrieve snow parameters based on the TOA radiances. For this purpose, we created a neural network that takes as input the sun-satellite geometry angles as well as the TOA radiances. The output will be the corresponding snow grain size, snow impurity concentration, visible albedo (VIS, 380–700 nm), near-infrared (NIR, 700–2500 nm) albedo, and visible shortwave infrared (VSWIR, 380–2500 nm) albedo. A multi-layer neural network (MLNN) is a feedforward artificial neural network used for pattern classification, recognition, prediction, and function approximation. It has been demonstrated that MLNNs with one or more hidden layers and a non-linear activation function can approximate nonlinear functions [36,37]. Therefore, it is suitable for solving our inverse problem, which is to derive the snow parameters and the VIS, NIR, and VSWIR albedo from the TOA radiances measured at a given set of wavelength bands for a specific sun-satellite geometry configuration, i.e., the solar zenith angle, the sensor observation angle, and the relative azimuth angle between the sun and the satellite sensor. When constructing an MLNN, one important issue is to find the optimum number of hidden layers and neurons. This determination depends on many variables, such as the number of neurons of the input and output layer, the number of training samples, the complexity of the function to be approximated, the type of activation function, and the training algorithm. This circumstance makes it difficult to find the best solution in many cases. Drawing on previous experience [38], we were able to find a suitable MLNN configuration, as described below.

3.1.1. Neural Network Setup

We used a network with five layers: one input layer, one output layer, and three hidden layers with 50, 30, and 20 neurons, respectively. The input layer uses three geometry angles and TOA radiances as inputs. The output layer contains a total of five outputs: snow grain size, snow impurity concentration, VIS albedo, NIR albedo, and VSWIR albedo. Three MLNNs were configured to employ TOA radiance channels similar to those used by the SBG, MODIS, and SGLI sensors. The continuous hyperspectral SBG MLNN used all 213 TOA radiance bands from 380 nm to 2500 nm, in 10 nm increments. To enable comparisons with existing multispectral sensors, such as MODIS and SGLI, a MODIS MLNN was constructed with seven TOA radiance bands (470 nm, 560 nm, 650 nm, 860 nm, 1240 nm, 1640 nm, and 2130 nm). Similarly, an SGLI MLNN was constructed with thirteen TOA radiance bands (380 nm, 410 nm, 440 nm, 490 nm, 530 nm, 570 nm, 670 nm, 760 nm, 870 nm, 1050 nm, 1380 nm, 1630 nm, and 2210 nm). A fourth Max-Min MLNN was formed using local maxima and minima of the radiance vs. wavelength and the albedo vs. wavelength (Figures 2 and 3). This approach led to an MLNN with forty-nine unique TOA radiance bands, with the majority of bands located between 600 nm and 1200 nm. Because we are using supervised learning, predictor inputs and desired output values were used to train the MLNN. Hence, we expect that the selection of predictor inputs for wavelengths producing the largest contrast in desired outputs (the local maxima and minima) should lead to an MLNN that easily learns the training data [39,40]. All MLNNs produced the same five parameters as outputs.

A hyperbolic tangent function was used as the neuron transfer (activation) function. A stochastic gradient descent method was used to minimize the cost function to obtain optimized weights and biases [41]. An adaptive learning rate, initially set to 0.001, was used for weight updates. A tolerance for optimization was set to 10^{-8}. When the loss function did not improve by at least this tolerance amount after ten consecutive iterations, convergence was considered to be reached and the training was terminated.

3.1.2. Training Results

From the 50,000 values in the synthetic snow dataset, 45,000 were used for MLNN training while the other 5000 were used for performance evaluation. Snow parameter

retrieval MLNN training completed with an average R^2 score across all parameters of 0.997 and a minimum band R^2 score of 0.992. The snow impurity parameter had the largest average percent error (APE) and bias of all the retrieval parameters. Training for albedo parameters and snow grain size performed well with all four MLNNs producing high R^2 scores (0.996 on average) and low APEs and bias. A different configuration of neurons in the hidden layers might have yielded better results, but the average R^2 scores already indicated that we had obtained an acceptable fit. MLNN training performance versus model synthetic data are shown in Figures 4–7 for the SBG, MODIS, SGLI, and Max-Min MLNNs.

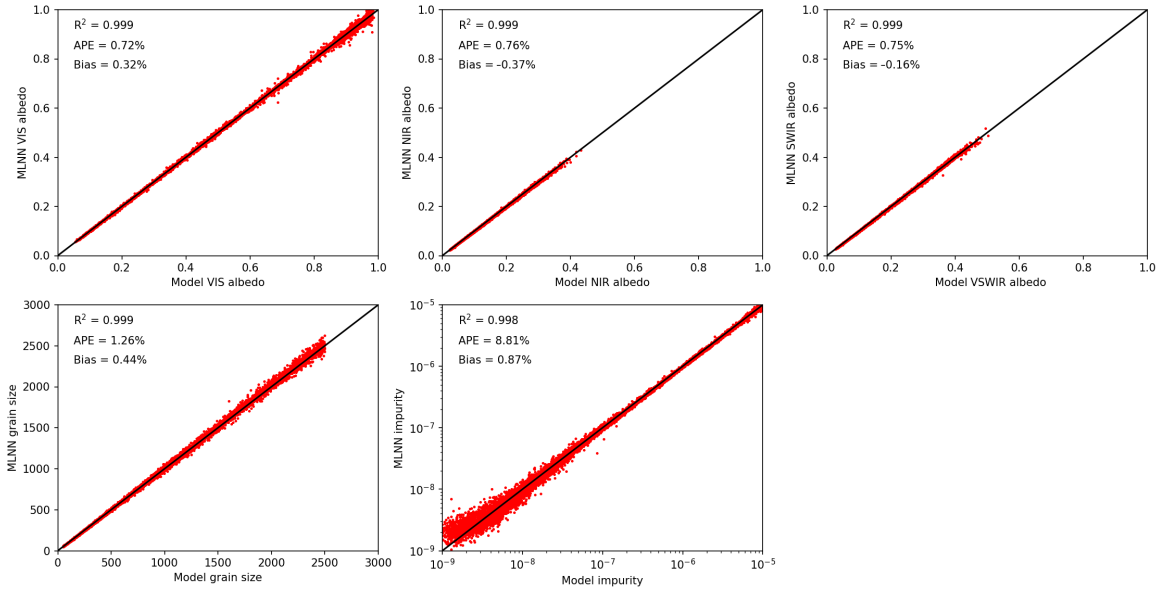

Figure 4. Results of SBG MLNN snow parameter training performance versus model synthetic data (N = 45,000).

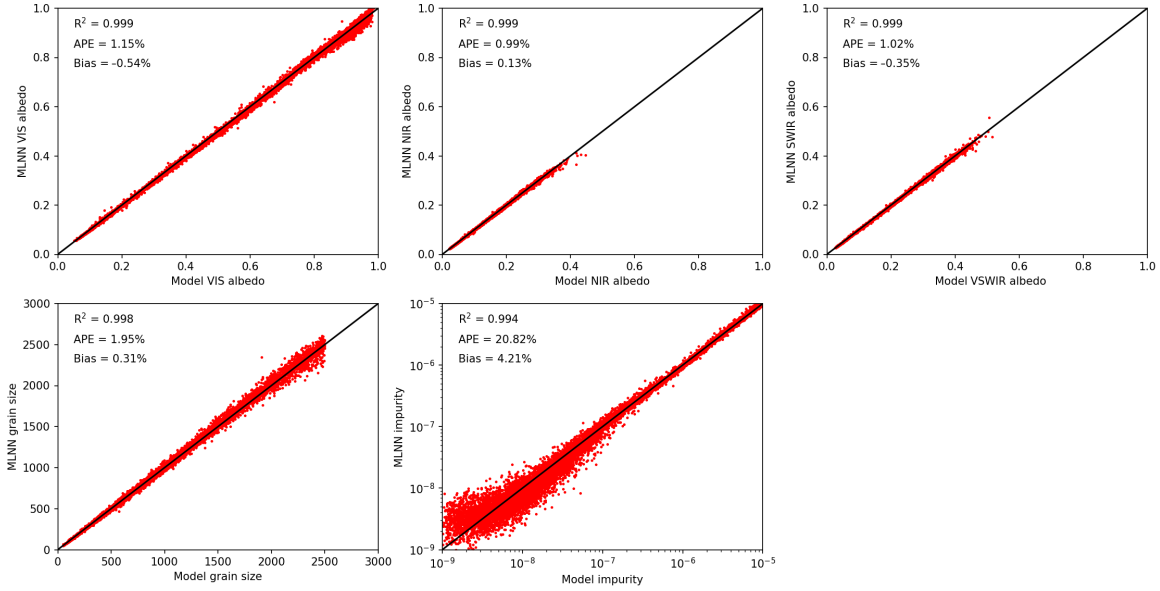

Figure 5. Results of MODIS MLNN snow parameter training performance versus model synthetic data (N = 45,000).

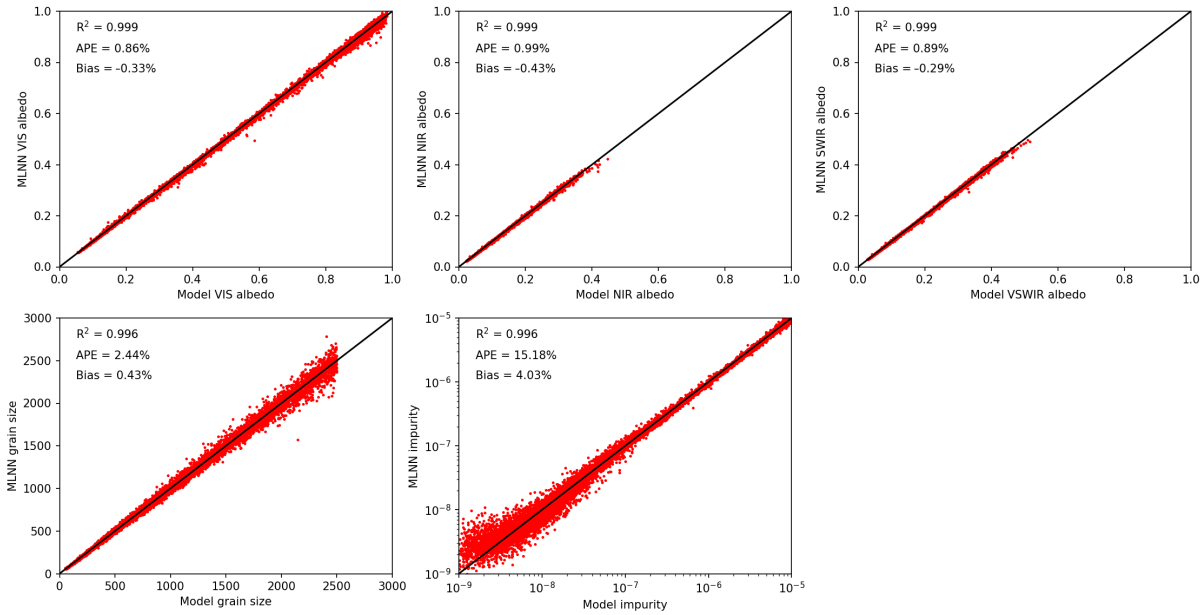

Figure 6. Results of SGLI MLNN snow parameter training performance versus model synthetic data (N = 45,000).

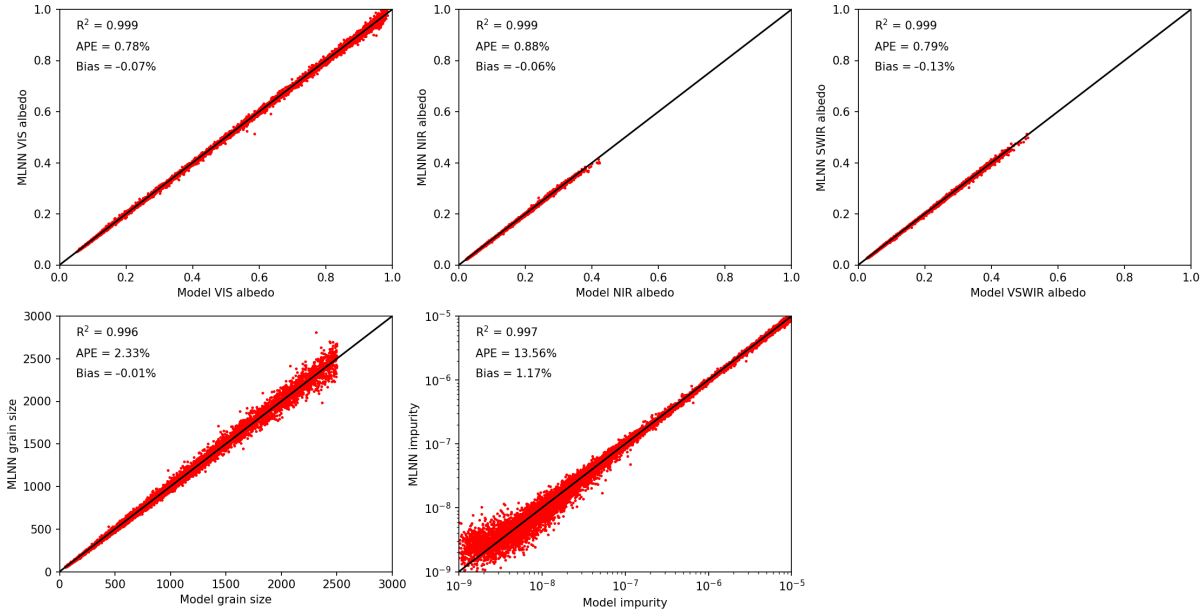

Figure 7. Results of Max-Min MLNN snow parameter training performance versus model synthetic data (N = 45,000).

3.1.3. Inversion Model

Weights and biases obtained from the training were saved and used to create approximation algorithms. The transfer (activation) function of the neurons was taken to be the hyperbolic tangent function:

$$f(x) = \frac{2}{1 + \exp[-2x]} - 1 = \frac{e^x - e^{-x}}{e^x + e^{-x}} = \tanh(x). \quad (1)$$

In the output layer, a linear transfer function was used to link the hidden layers to the output. The exact expression of this MLNN approximation algorithm can be written as:

$$y_m = b_{4,m} + \sum_{l=1}^{N_3} w_{4,ml} \cdot f\left\{ b_{3,l} + \sum_{k=1}^{N_2} w_{3,lk} \cdot f\left[b_{2,k} + \sum_{j=1}^{N_1} w_{2,kj} \cdot f\left(b_{1,j} + \sum_{i=1}^{N_0} w_{1,ji} \cdot x_i \right) \right] \right\} \quad (2)$$

where x_i, $i = 1, \ldots, N_0$ is an element in the input layer.

In Equation (2), $w_{1,ji}$ are the weights of the input layer, $w_{2,kj}$, $w_{3,lk}$, and $w_{4,ml}$ are the weights of the three hidden layers, $b_{1,j}$ is the bias of the input layer, $b_{2,k}$, $b_{3,l}$, and $b_{4,m}$ are the biases of the three hidden layers. f is the hyperbolic tangent function in Equation (1). y_m is the mth element in the output layer, which in our case contains the snow grain size, snow impurity concentration, VIS albedo, NIR albedo, and VSWIR albedo.

4. Results and Discussion

4.1. Results

The main criterion used to evaluate the performance of each algorithm is accuracy, which we define based on how close each predicted (retrieved) value is to its corresponding synthetic model value. To determine accuracy, we use the average percent difference (APD), the difference between our predicted value and the model value in comparison to the model value (relative error), and the mean absolute error (MAE), based on the difference between the predicted value and the synthetic model value. A summary of the performance of the four snow parameter retrieval algorithms is shown in Table 2. Overall, all of the algorithms performed well for retrievals of the albedo and snow grain size. The SBG algorithm offers improvements over the other algorithms for retrieval of the snow impurity concentration, having the best R^2 score and the lowest average percent difference (5.6% for SBG, versus 14%, 9.4%, and 7.8% for MODIS, SGLI, and Max-Min) and mean absolute error. The SGLI, MODIS, and Max-Min algorithms struggled to reliably estimate snow impurities in the 10^{-9} to 10^{-8} ranges, leading to a worse performance than the SBG algorithm in this range. Evaluation of the performance of SBG, MODIS, SGLI, and Max-Min prediction algorithms against synthetic data is shown in Figures 8–11.

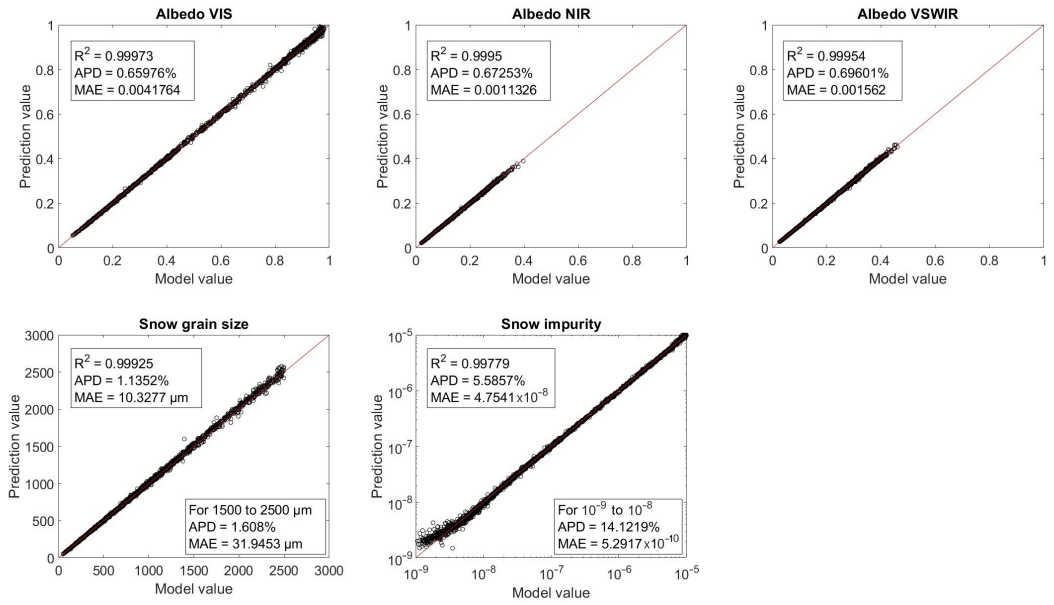

Figure 8. Performance of SBG snow parameter retrieval algorithm predictions versus model synthetic data (N = 5000).

Table 2. A summary of the performance of the three snow parameter retrieval algorithms based on R^2 score, APD, and MAE.

SBG Algorithm	R^2 Score	APD	MAE
Albedo VIS	0.999	0.660 %	0.004
Albedo NIR	0.999	0.673 %	0.001
Albedo VSWIR	0.999	0.670 %	0.002
Snow grain size	0.999	1.135 %	10.33 µm
Snow impurity	0.998	5.586 %	4.754×10^{-8}
MODIS algorithm	**R^2 Score**	**APD**	**MAE**
Albedo VIS	0.999	1.025 %	0.006
Albedo NIR	0.999	0.914 %	0.001
Albedo VSWIR	0.999	0.943 %	0.002
Snow grain size	0.998	1.602 %	14.78 µm
Snow impurity	0.997	13.99 %	8.907×10^{-8}
SGLI algorithm	**R^2 Score**	**APD**	**MAE**
Albedo VIS	0.999	0.699 %	0.004
Albedo NIR	0.999	0.809 %	0.001
Albedo VSWIR	0.999	0.744 %	0.002
Snow grain size	0.998	1.610 %	14.52 µm
Snow impurity	0.997	9.34 %	6.148×10^{-8}
Max-Min algorithm	**R^2 Score**	**APD**	**MAE**
Albedo VIS	0.999	0.618 %	0.004
Albedo NIR	0.999	0.688 %	0.001
Albedo VSWIR	0.999	0.641 %	0.002
Snow grain size	0.998	1.545 %	14.02 µm
Snow impurity	0.998	7.829 %	5.336×10^{-8}

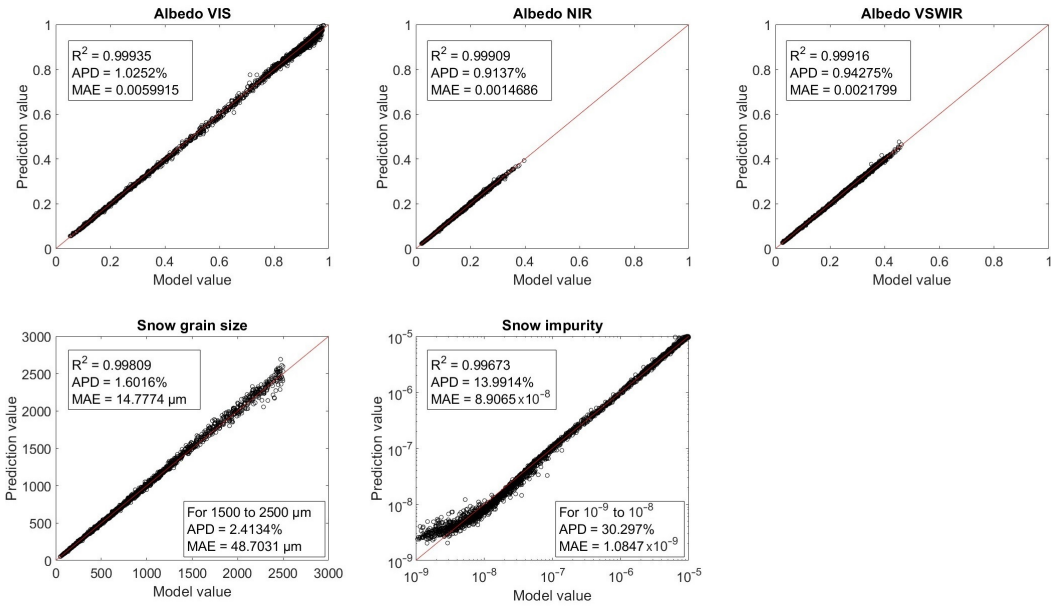

Figure 9. Performance of MODIS snow parameter retrieval algorithm predictions versus model synthetic data (N = 5000).

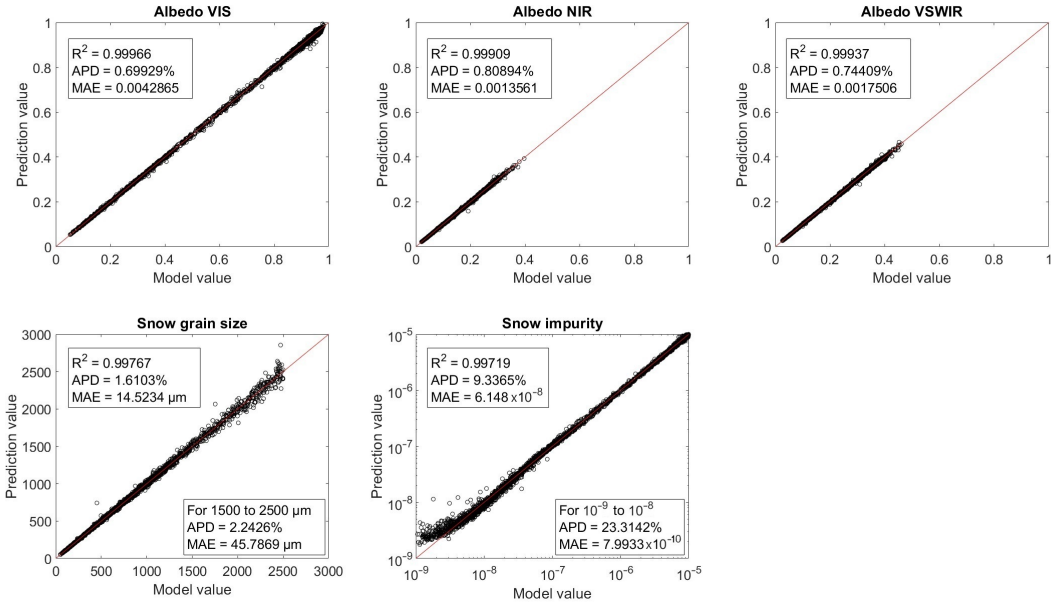

Figure 10. Performance of SGLI snow parameter retrieval algorithm predictions versus model synthetic data (N = 5000).

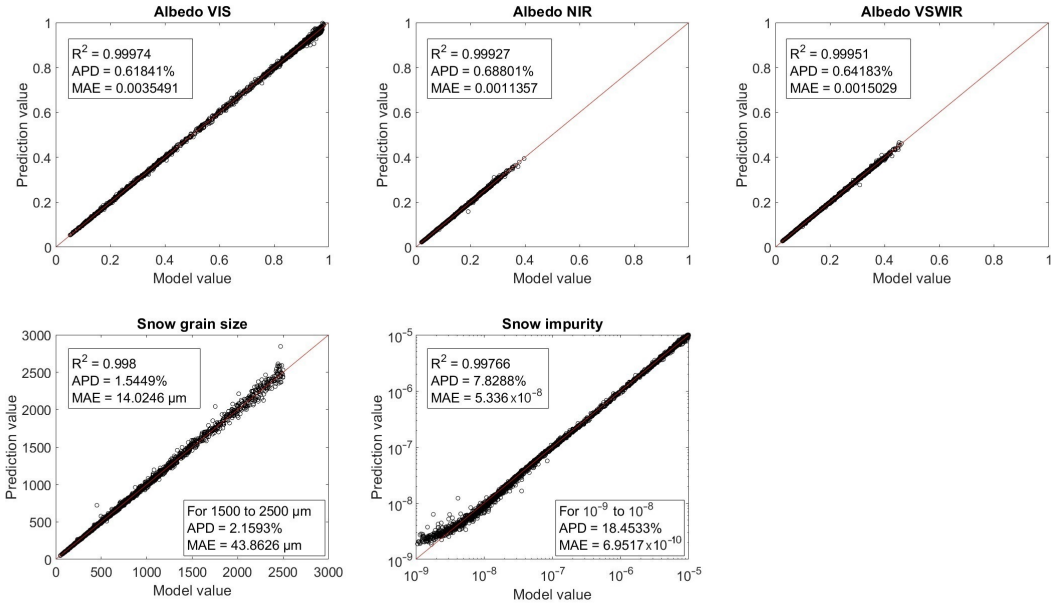

Figure 11. Performance of Max-Min snow parameter retrieval algorithm predictions versus model synthetic data (N = 5000).

4.2. Discussion

Our sensitivity study's findings indicate that using continuous (hyperspectral) channels when developing an SPR algorithm offers some improvements over selecting specific (multispectral) wavelengths like those available for sensors such as MODIS and SGLI. It is likely that the SBG algorithm outperformed the other three algorithms when it comes to snow impurity because of its channel configuration. Figure 2E shows that for impurity values in the 10^{-9} to 10^{-8} range, radiances in the 380–600 nm range are significantly affected by the impurity, while the impact is insignificant at longer wavelengths. The SBG algorithm has twenty-three channels in this spectral range, while the Min-Max and SGLI algorithms have six channels and the MODIS algorithm has only two. Both the MODIS,

Figure 9, and SGLI, Figure 10, algorithms tended to overestimate very low impurity values and underestimate values near and around 10^{-8}, leading to an S-like curve in the plots. This tendency is most noticeable for the MODIS algorithm where the underestimation continues past 10^{-8} up to 10^{-7}. To a lesser extent, this S-like curving is also present in the Max-Min plots shown in Figure 11. The SBG algorithm, Figure 8, performed better in these ranges with an APD of 14.1% compared to 30.3%, 23.3%, and 18.5% for MODIS, SGLI, and Max-Min, respectively. However, the SBG algorithm still overestimates very low impurities near 10^{-9}.

The use of channels based on a continuous spectrum configuration also shows small improvements in predicting snow grain size. When comparing the SBG algorithm to the other algorithms, we observe a tighter grouping of data in the SBG plots (Figure 8). This tighter clustering becomes more noticeable as snow grain size increases, with the SBG algorithm having an MAE of 31.9 µm for snow grains ranging from 1500 to 2500 µm compared to 48.7 µm, 45.8 µm, and 43.9 µm for the MODIS, SGLI, and Max-Min algorithms. Figure 2D shows that the variation in radiance across all wavelengths becomes less pronounced as the grain size increases. We observe a much larger shift when grain sizes increase from 50 to 300 µm than for when it increases from 900 to 2500 µm. This behavior likely made it harder for the MLNNs to precisely evaluate changes in radiance caused by large snow grains, leading to a larger deviation of prediction values from the model data for large grain sizes for the three multi-band algorithms.

All four algorithms were able to accurately predict the albedo in the visible, near-infrared, and shortwave infrared spectral ranges. The reason is likely that the variation of albedo vs. wavelengths is much smoother than the variation of radiance vs. wavelength, making the albedo easy to predict from only a few wavelength channels. However, since the albedo mainly depends on the physical properties of snow, to get an understanding of the global climate system it is not enough to solely predict this value. It is possible that a snow sample with small grain size and high impurity could produce the same albedo as a different snow sample with large grain size and low impurity. An illustration of this circumstance is shown in Figure 12. Despite the large differences in grain sizes and impurity concentrations, the two very different snow configurations are shown to yield the same VSWIR (380–2500 nm) albedo.

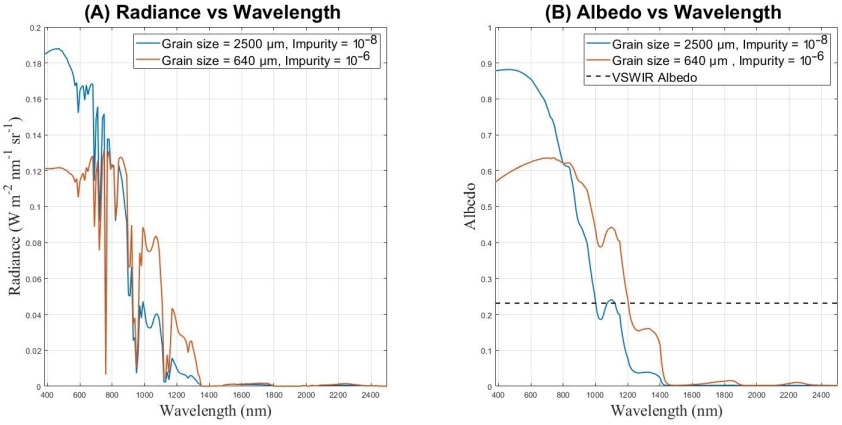

Figure 12. Radiance vs. wavelength (**A**) and albedo vs. wavelength (**B**) for two simulated samples, both with the same relative azimuthal angle of 90°, viewing zenith angle of 22.5°, and solar zenith angle of 45°. The blue line has grain size of 2500 µm and impurity concentration of 10^{-8}, while the red line has grain size of 640 µm, and impurity concentration of 10^{-6}. Both samples have the same VSWIR (380–2500 nm) albedo of 0.231, shown by the dashed black line.

The Max-Min algorithm contains channels at all of the peaks and valleys observed in our illustration plots, Figures 2 and 3. These channels should contain the most contrasting values and make it easy for a neural network to identify differences in retrieval parameters. If a continuous spectrum then contained redundant channels, we would expect the SBG

algorithm and Max-Min algorithm to perform similarly. However, there appears to be a marked improvement in accuracy when using continuous spectral coverage. While the Max-Min algorithm performed better than the other two multi-band approaches, it shares their discrepancies between predicted values and model data for large snow grain sizes and the same tendency to overestimate small impurity concentrations.

Since changes in grain size, impurity, and geometry angles all affect the TOA radiance in unique ways, it is perhaps not surprising that having more spectral channels leads to increased accuracy. Our results point to better neural network training and prediction algorithm performance when continuous spectral coverage is utilized. However, equidistant spectral sampling, such as that proposed/envisioned for SBG, does not necessarily guarantee optimum performance. It seems reasonable to expect that placing more sampling points in spectral regions with steep gradients than in regions where the spectrum is relatively flat could be beneficial.

5. Conclusions

We have explored the impact of physical snow properties on TOA spectral radiance and how machine learning neural networks could be used to form a snow parameter retrieval algorithm utilizing multi-band and continuous (hyperspectral) coverage. We have determined that employing continuous spectral coverage, such as that offered by the planned SBG VSWIR instrument, seems to offer some improvements to the quality of snow parameter retrievals when compared with multi-band approaches, used by sensors such as MODIS and SGLI, by lowering the APD and MAE for snow grain size and snow impurity concentration. While our study focused on snow parameter retrieval in a single homogeneous snow layer, continuous (hyper) spectral coverage will likely show even more improvements for a vertically inhomogeneous snow-pack consisting of multiple dissimilar layers. An area of future research could be exploring how the improvements observed in our sensitivity study offered by continuous spectral coverage affects parameter retrieval in more diverse systems, such as systems with vertically inhomogeneous snow grain size and impurity profiles, as well as snow systems containing "contaminants" such as algae and mineral particles. Another avenue of research could be exploring benefits offered to cloud screening of optical imagery involving snow. Continuous spectral coverage offers increased degrees of freedom for machine learning algorithms to understand and quantify complex systems, which makes sensors with continuous spectral coverage a good choice for future remote sensing endeavors. The hyperspectral SPR algorithm developed and tested in this study showed promising results when used with simulated data. However, it must be developed further and tested against real snow spectral data. The JPL AVIRIS, AVIRIS-NG, and PRISM airborne imaging spectrometers have collected such data. It would be a logical next step to use such data to test the capabilities of our SPR algorithm.

Author Contributions: Individual research contributions: Conceptualization, K.S. and C.G.; methodology, W.L. and E.P.; validation, E.P. and W.L.; writing—original draft preparation, E.P.; writing—review and editing, K.S. and T.T.; visualization, E.P.; supervision, W.L and K.S.; project administration, K.S.; funding acquisition, C.G. All authors have read and agreed to the published version of the manuscript.

Funding: This research was funded in part by NASA/AMES Research Cooperative Agreement No. NASA-NNX12AD05A, CFDA No. 43.001 through Bay Area Environmental Research Institute.

Data Availability Statement: Data used in this paper are available upon request, please contact the corresponding author with any inquiries.

Conflicts of Interest: The authors declare that the research was conducted in the absence of any commercial or financial relationships that could be construed as potential conflict of interest.

References

1. Frei, A.; Tedesco, M.; Lee, S.; Foster, J.; Hall, D.; Kelly, R.; Robinson, D. A review of global satellite-derived snow products. *Adv. Space Res.* **2012**, *50*, 1007–1029. [CrossRef]
2. Deltz, A.; Kruenzer, C.; Gessner, U.; Dech, S. Remote sensing of snow—A review of available methods. *Int. J. Remote Sens.* **2012**, *33*, 4094–4134.
3. Tedesco, M. *Remote Sensing of the Cryosphere*; Wiley: New York, NY, USA, 2015
4. Stamnes, K.; Li, W.; Eide, H.; Aoki, T.; Hori, M.; Storvold, R. ADEOS-II/GLI snow/ice products: Part I-Scientific basis. *Remote Sens. Environ.* **2007**, *111*, 258–273. [CrossRef]
5. Lyapustin, A.; Tedesco, M.; Wang, Y.; Aoki, T.; Hori, M.; Kokhanovsky, A. Retrieval of snow grain size over greenland from modis. *Remote Sens. Environ.* **2009**, *113*, 1976–1987. [CrossRef]
6. Zege, E.; Katsev, I.; Malinka, A.; Prikhach, A.; Heygster, G.; Wiebe, H. Algorithm for retrieval of the effective snow grain size and pollution amount from satellite measurements. *Remote Sens. Environ.* **2011**, *115*, 2674–2685. [CrossRef]
7. Kokhanovsky, A.; Lamare, M.; Danne, O.; Brockmann, C.; Dumont, M.; Brockmann, C.; Picard, G.; Arnaud, L.; Favier, V.; Jourdain, B.; et al. Retrieval of snow properties from the sentinel-3 ocean and land colour instrument. *Remote Sens.* **2019**, *11*, 2280. [CrossRef]
8. Cawse-Nicholson, K.; Townsend, P.A.; Schimel, D.; Assiri, A.M.; Blake, P.L.; Buongiorno, M.F.; Campbell, P.; Carmon, N.; Casey, K.A.; Correa-Pabó, R.E.; et al. NASA's surface biology and geology designated observable: A perspective on surface imaging algorithms. *Remote Sens. Environ.* **2021**, *257*, 112349. [CrossRef]
9. National Academies of Sciences Engineering Medicine. *Thriving on Our Changing Planet: A Decadal Strategy for Earth Observation from Space*; The National Academies Press: Washington, DC, USA, 2018.
10. Rittger, K.; Painter, T.; Dozier, J. Assessment of methods for mapping snow cover from MODIS. *Adv. Water Resour.* **2013**, *51*, 367–380. [CrossRef]
11. Kokhanovsky, T.; Shimada, R.; Aoki, T.; Hori, M. The determination of snow parameters using SGLI/GCOM-C spaceborne top-of-atmosphere spectral reflectance measurements over Antarcticar. *J. Quant. Spectrosc. Radiat. Transf.* **2022**, *287*, 108226. [CrossRef]
12. Hori, M.; Sugiura, K.; Kobayashi, K.; Aoki, T.; Tanikawa, T.; Kuchiki, K.; Niwano, M.; Enomoto, H. A 38-year (1978–2015) Northern Hemisphere daily snow cover extent product derived using consistent objective criteria from satellite-borne optical sensors. *Remote Sens. Environ.* **2017**, *191*, 402–418. [CrossRef]
13. Thompson, D.; Natraj, V.; Green, R.; Helmlinger, M.; Gao, B.; Eastwood, M. Optimal estimation for imaging spectrometer atmospheric correction. *Remote Sens. Environ.* **2018**, *216*, 355–373. [CrossRef]
14. Painter, T.; Seidel, F.; Bryant, A.; Skiles, S.; Rittger, K. Imaging spectroscopy of albedo and radiative forcing by light-absorbing impurities in mountain snow. *J. Geophys. Res.-Atmos.* **2013**, *118*, 9511–9523. [CrossRef]
15. Gubler, H. Model of dry snow metamorphism by interparticle vapor flux. *J. Geophys. Res.* **1985**, *90*, 8081–8092. [CrossRef]
16. Langham, E. Physics and properties of snowcover. In *Handbook of Snow, Principles, Processes, Management and Use*; Pergamon Press: Oxford, UK, 1981; pp. 275–337.
17. Male, D.; Gray, D. Snowcover ablation and runoff. In *Handbook of Snow, Principles, Processes, Management and Use*; Pergamon Press: Oxford, UK, 1981; pp. 360–436.
18. Palm, E.; Tveitereid, M. On heat and mass flow through dry snow. *J. Geophys. Res.* **1979**, *84*, 745–749. [CrossRef]
19. Colbeck, S. Theory of metamorphism of dry snow. *J. Geophys. Res.* **1983**, *88*, 5475–5482. [CrossRef]
20. Budd, W.; Dingle, W.; Radok, U. The Byrd snow drift project: Outline and basic results. *Stud. Antarct. Meteorol. Am. Geophys. Union Antarct. Res. Ser.* **1966**, *9*, 71–134.
21. Schmidt, R.; Troendle, C. Sublimation of intercepted snow as a global source of water vapour. In Proceedings of the 60th Annual Western Snow Conference, Jackson Hole, WY, USA, 14–16 April 1992; pp. 1–9.
22. Marsh, P.; Woo, M. Wetting front advance and freezing of meltwater within a snowcover 1. Observations in the Canadian Arctic. *Water Resources Res.* **1984**, *20*, 1853–1864. [CrossRef]
23. Laszlo, I.; Liu, H.; Kim, H.Y.; Pinker, R.T. *Chapter 15-Shortwave Radiation from ABI on the GOES-R Series*; The GOES-R Series; Goodman, S.J., Schmit, T.J., Daniels, J., Redmon, R.J., Eds.; Elsevier: Amsterdam, The Netherlands, 2020; pp. 179–191.
24. Wiscombe, W.; Warren, S. A Model for the Spectral Albedo of Snow. I: Pure Snow. *J. Atmos. Sci.* **1980**, *37*, 2712–2733. [CrossRef]
25. Warren, S.; Wiscombe, W. A Model for the Spectral Albedo of Snow. II: Snow Containing Atmospheric Aerosols. *J. Atmos. Sci.* **1980**, *37*, 2734–2745. [CrossRef]
26. O'Neil, A.; Gray, D. Spatial and temporal variations of the albedo of a prairie snowpack. In *The Role of Snow and Ice in Hydrology: Proceedings of the Bang Symposium*; Unesco-WMO-IAHS: Paris, France, 1973; pp. 176–186.
27. Stamnes, K.; Hamre, B.; Stamnes, S.; Chen, N.; Fan, Y.; Li, W.; Lin, Z.; Stamnes, J. Progress in forward-inverse modeling based on radiative transfer tools for coupled atmosphere-snow/ice-ocean systems: A review and description of the AccuRT model. *Appl. Sci.* **2018**, *8*, 2682. [CrossRef]
28. Wang, W.; Dungan, J.; Genovese, V.; Shinozuka, Y.; Yang, Q.; Liu, X.; Poulter, B.; Brosnan, I. Development of the Ames Global Hyperspectral Synthetic Data Set: Surface Bidirectional Reflectance Distribution Function. *J. Geophys. Res. Biogeosci.* **2023**, *128*, e2022JG007363. [CrossRef]

29. Thuillier, G.; Herse, M.; Labs, D.; Foujols, T.; Peetermans, W.; Gillotay, D.; Simon, P.; Mandel, H. The Solar Spectral Irradiance from 200 to 2400 nm as Measured by the SOLSPEC Spectrometer from the Atlas and Eureca Missions. *Sol. Phys.* **2003**, *214*, 1–22. [CrossRef]
30. Anderson, G.; Chetwynd, J.; Wang, J.; Hall, L.; Kneizys, F.; Kimball, L.; Bernstein, L.; Acharya, P.; Berk, A.; Robertson, D.; et al. MODTRAN 3: Suitability as a flux-divergence code. In Proceedings of the 4th ARM Science Team Meeting, Charleston, SC, USA, 28 February–3 March 1994; pp. 75–80.
31. *ATSM Standard G173-03*; Standard Tables for Reference Solar Spectral Irradiances: Direct Normal and Hemispherical on 37° Tilted Surfac. ASTM International: West Conshohocken, PA, USA, 2020; Volume 114, pp. 1–21.
32. Anderson, G.; Clough, S.; Kneizys, F.; Chetwynd, J.; Shettle, E. *AFGL Atmospheric Constituent Profiles (0–120 km)*; AFGL-TR-86-0110; Air Force Geophysics Laboratory: Hanscom, MA, USA, 1986; p. 01736.
33. Kassianov, E.; Cromwell, E.; Monroe, J.; Riihimaki, L.; Flynn, C.; Barnard, J.; Michalsky, J.J.; Hodges, G.; Shi, Y.; Comstock, J.M. Harmonized and high-quality datasets of aerosol optical depth at a US continental site, 1997–2018. *Sci. Data* **2021**, *8*, 82. [CrossRef] [PubMed]
34. Stamnes, K.; Hamre, B.; Stamnes, J.; Ryzhikov, G.; Birylina, M.; Mahoney, R.; Hauss, B.; Sei, A. Modeling of radiation transport in coupled atmosphere-snow-ice-ocean systems. *J. Quant. Spectrosc. Radiat. Transf.* **2011**, *112*, 714–726. [CrossRef]
35. Grenfell, T.; Warren, S.; Mullen, P. Reflection of solar radiation by the Antarctic snow surface at ultraviolet, visible, and near-infrared wavelengths. *J. Geophys. Res.* **1994**, *99*, 669–684. [CrossRef]
36. Chen, S.; Billings, S.; Grant, P. Non-linear system identification using neural networks. *Int. J. Control* **1990**, *51*, 1191–1214. [CrossRef]
37. D'Alimonte, D.; Zibordi, G. Phytoplankton determination in an optically complex coastal region using a multilayer perceptron neural network. *IEEE Trans. Geosci. Remote Sens.* **2003**, *41*, 2861–2868. [CrossRef]
38. Fan, Y.; Li, W.; Chen, N.; Ahn, J.; Park, Y.; Kratzer, S.; Schroeder, T.; Ishizaka, J.; Chang, R.; Stamnes, K. OC-SMART: A machine learning based data analysis platform for satellite ocean color sensors. *Remote Sens. Environ.* **2021**, *253*, 112236. [CrossRef]
39. Jiang, T.; Gradus, J.; Rosellini, A. Supervised Machine Learning: A Brief Primer. *Behav. Ther.* **2020**, *51*, 675–687. [CrossRef]
40. Mayer, N.; Ilg, E.; Fischer, P.; Hazirbas, C.; Cremers, D.; Dosovitskiy, A.; Brox, T. What Makes Good Synthetic Training Data for Learning Disparity and Optical Flow Estimation? *CoRR* **2018**, *126*, 942–960. [CrossRef]
41. Diederik, P.; Ba, J. Adam: A Method for Stochastic Optimization. *arXiv* **2015**, arXiv:1412.6980.